Chinese Physics Letters **41**, 074205 (2024) **Express Letter**

Manipulating the Spatial Structure of Second-Order Quantum Coherence Using Entangled Photons

Shuang-Yin Huang(黄双印)[1,2†], Jing Gao(高菁)[1,2†], Zhi-Cheng Ren(任志成)[1,2], Zi-Mo Cheng(程子默)[1,2], Wen-Zheng Zhu(朱文正)[1,2], Shu-Tian Xue(薛舒天)[1,2], Yan-Chao Lou(娄严超)[1,2], Zhi-Feng Liu(刘志峰)[1,2], Chao Chen(陈超)[1,2*], Fei Zhu(朱飞)[3], Li-Ping Yang(杨立平)[4*], Xi-Lin Wang(汪喜林)[1,2,5,6*], and Hui-Tian Wang(王慧田)[1,2,7]

[1]*National Laboratory of Solid State Microstructures and School of Physics, Nanjing University, Nanjing 210093, China*
[2]*Collaborative Innovation Center of Advanced Microstructures, Nanjing University, Nanjing 210093, China*
[3]*Intelligent Scientific Systems Co. Limited, Beijing 102208, China*
[4]*Center for Quantum Sciences and School of Physics, Northeast Normal University, Changchun 130024, China*
[5]*Hefei National Laboratory, Hefei 230088, China*
[6]*Synergetic Innovation Center of Quantum Information and Quantum Physics, University of Science and Technology of China, Hefei 230026, China*
[7]*Collaborative Innovation Center of Extreme Optics, Shanxi University, Taiyuan 030006, China*

(Received 14 May 2024; accepted manuscript online 21 June 2024)

High-order quantum coherence reveals the statistical correlation of quantum particles. Manipulation of quantum coherence of light in the temporal domain enables the production of the single-photon source, which has become one of the most important quantum resources. High-order quantum coherence in the spatial domain plays a crucial role in a variety of applications, such as quantum imaging, holography, and microscopy. However, the active control of second-order spatial quantum coherence remains a challenging task. Here we predict theoretically and demonstrate experimentally the first active manipulation of second-order spatial quantum coherence, which exhibits the capability of switching between bunching and anti-bunching, by mapping the entanglement of spatially structured photons. We also show that signal processing based on quantum coherence exhibits robust resistance to intensity disturbance. Our findings not only enhance existing applications but also pave the way for broader utilization of higher-order spatial quantum coherence.

DOI: 10.1088/0256-307X/41/7/074205

High-order coherence of light reveals the statistical correlation beyond the first-order coherence indicated by intensity fringes in traditional interference (such as the best-known Young's double-slit interference). Study on high-order coherence was pioneered by Hanbury Brown and Twiss (HBT) in a landmark interferometric experiment in 1956,[1] in which the bunching of photons in thermal light was observed. This discovery led Glauber to lay the foundation of quantum optics by developing the quantum theory of coherence[2] and found practical application in astronomy to measure the angular diameter of stars.[3] Since then, the HBT interferometry has been deeply explored with various sources, such as interacting photons in a nonlinear medium[4] and twisted light,[5] and has attracted significant interest beyond photons, including electrons (anti-bunching effect for fermions),[6,7] atoms,[8–10] molecules,[11] matter wave,[12] and phonons.[13]

In contrast to the thermal source, the high-order coherence of quantum light unveils remarkable statistical behaviors among quantum particles. As a typical quantum source, single-photon source[14–17] shows the antibunching effect in the temporal domain and has important applications ranging from quantum foundation,[18,19] quantum communications,[20] quantum metrology[21,22] to quantum computation and quantum simulation.[23,24] The bunching and antibunching behaviors of photons are usually described by the degree of second-order quantum coherence in temporal domain, which is quantified by $g^{(2)}(\tau)$, where $\tau = t_2 - t_1$ is the arriving time difference between two detected photons. A perfect single-photon source has a vanishing $g^{(2)}(\tau)|_{\tau=0} = 0$, indicating its intrinsic "single-photon" nature, as shown in Fig. 1(a). The anti-bunching effect, meaning $g^{(2)}(\tau)|_{\tau=0} < 1$, originates from sub-Poissonian photon statistics[25] and signifies a genuine quantum phenomenon with no classical counterpart. The control of high-order quantum coherence in *temporal domain* has brought significant impacts on quantum information and quantum optics. Consequently, actively manipulating this quantum feature in *spatial domain* is expected to find new quantum effects, phenomena, and applications.

The spatial correlation of both quantum[26–29] and classical[30–32] light has been extensively explored, particularly in the correlated-photon imaging.[33–39] Furthermore, spatially structured entangled photons have been achieved by establishing entanglement in spatial degree of freedom (DOF),[40–45] for example, orbital angular mo-

†These authors contributed equally to this work.
*Corresponding authors. Email: chaochen@nju.edu.cn; lipingyang87@gmail.com; xilinwang@nju.edu.cn
© 2024 Chinese Physical Society and IOP Publishing Ltd

mentum (OAM) arising from a helical phase of $\exp(jm\varphi)$ (where φ is the azimuthal angle in the polar coordinates and the integer index m indicates the topological charge). The quantum feature from the spatial structure can be utilized to produce various types of entanglement, such as two-photon [46] and multi-photon [47–51] high-dimensional entanglement, high-OAM entanglement [52,53] and hyperentanglement in multiple DOFs. [54–56] These novel quantum entanglements have found many important applications in various quantum information operations and protocols, such as Bell state measurement, [57,58] new quantum communication, [59,60] direct characterization of quantum dynamics, [61] quantum teleportation of multiple DOFs of a single photon, [62] measurement of particle exchange phase, [63] and characterization of Wigner distribution of twisted single photons. [64] The spatial structure in high-order quantum coherence holds great potential for intriguing effects and significant applications. However, on-demand manipulation of achieving high-order spatial quantum coherence remains challenging.

In this work, we theoretically propose and experimentally demonstrate the active control of second-order spatial quantum coherence of spatially structured entangled photons, as shown in Fig. 1(b). There are two physical quantities related to second-order spatial quantum coherence of photon pairs, i.e., second-order spatial quantum correlation function $G^{(2)}(\boldsymbol{r}, \boldsymbol{r}')$ and degree of second-order spatial quantum coherence $g^{(2)}(\boldsymbol{r}, \boldsymbol{r}')$. [2] $g^{(2)}(\boldsymbol{r}, \boldsymbol{r}')$ has unique feature different from $G^{(2)}(\boldsymbol{r}, \boldsymbol{r}')$. In theory, we develop an approach that maps the entanglement of spatially structured photons to the second-order spatial quantum coherence, which has good scalability for two and more entangled photons. In experiment, our approach is verified by measuring $g^{(2)}(\boldsymbol{r}, \boldsymbol{r}')$ of spatially entangled photon pair. The key to our experiment is to transfer the polarization entanglement of two momentum-uncorrelated photons to the spatially structured entanglement. Our results have the potential to pave the way for new possibilities in quantum information and enhance the control over photon-based systems.

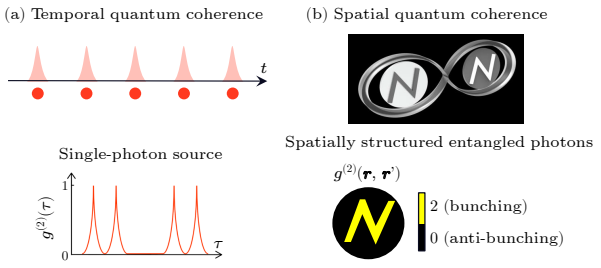

Fig. 1. Second-order temporal quantum coherence versus second-order spatial quantum coherence. (a) Degree of second-order temporal quantum coherence $g^{(2)}(\tau)$ is used to describe the bunching and antibunching statistics in temporal domain. (b) Degree of second-order spatial quantum coherence $g^{(2)}(\boldsymbol{r}, \boldsymbol{r}')$ characterizes the quantum spatial correlations of spatially structured entangled photons.

Active Manipulation of Spatial Quantum Coherence. Our control method for spatial quantum coherence lies in the conversion of global polarization entanglement into spatial one. Two photons are initially prepared in a polarization-entangled state of $\frac{1}{\sqrt{2}}(|H_A\rangle|V_B\rangle \pm |V_A\rangle|H_B\rangle)$ (H/V indicates horizontal/vertical polarization). By using the entanglement transfer unit (ETU) shown in Fig. 2 and appropriately selecting polarization coincidence channels, the statistical properties of the two photons can be actively manipulated through the carefully designed structured-phase entanglement [65,66] (see the Supplementary Material)

$$\Psi(\boldsymbol{r}, \boldsymbol{r}') \propto \eta_A(\boldsymbol{r})\eta_B(\boldsymbol{r}') \times \left\{ e^{j[\Phi_A(\boldsymbol{r}) - \Phi_B(\boldsymbol{r}')]} \pm e^{-j[\Phi_A(\boldsymbol{r}) - \Phi_B(\boldsymbol{r}')]} \right\}, \quad (1)$$

where $\eta_i(\cdot)$ ($i = \{A, B\}$) is the probability amplitude distribution of the paraxial photons in path i. By engineering the spatial structures of phases $\Phi_A(\boldsymbol{r})$ and $\Phi_B(\boldsymbol{r}')$, we can precisely control the spatial structure of $g^{(2)}(\boldsymbol{r}, \boldsymbol{r}')$ (see the Supplementary Material for details):

$$g^{(2)}(\boldsymbol{r}, \boldsymbol{r}') = \frac{G^{(2)}(\boldsymbol{r}, \boldsymbol{r}')}{n_A(\boldsymbol{r})n_B(\boldsymbol{r}')} = 1 \pm \cos[2\Phi_A(\boldsymbol{r}) - 2\Phi_B(\boldsymbol{r}')]. \quad (2)$$

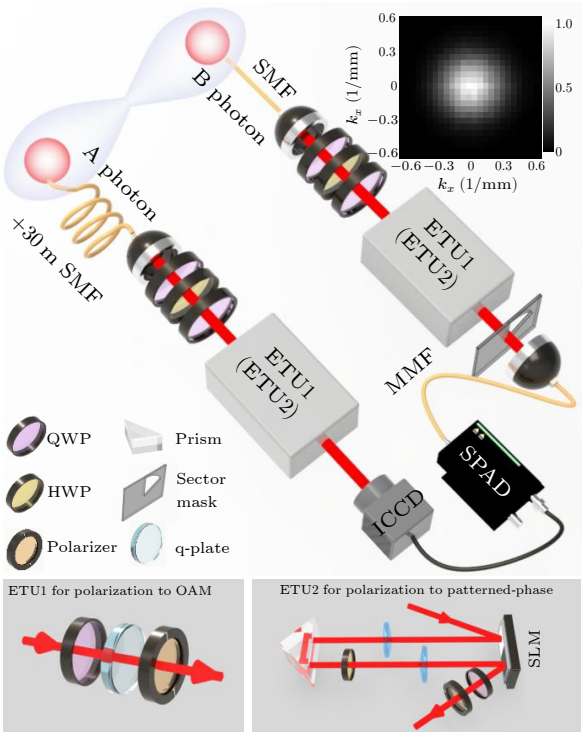

Fig. 2. Experimental setup of manipulating the spatial structure of second-order quantum coherence of spatially structured entangled photons. The momentum and frequency correlations of the photon pair are eliminated, as shown in the upper-right inset. The two-photon polarization entanglement is converted into either OAM entanglement or patterned-phase entanglement via entanglement transfer units (ETUs), which behave as polarization-dependent mode-switching devices, as shown in the lower two insets, ETU1 and ETU2 correspond to the polarization to OAM (continuously varying phase) and the polarization to patterned phase (discrete phase), respectively.

During the entanglement transfer, the intensity spatial distribution for photons in each path, measured in

the selected polarization channel, remains unchanged, i.e., $n_{\rm A}(\boldsymbol{r}) \propto |\eta_{\rm A}(\boldsymbol{r})|^2$ and $n_{\rm B}(\boldsymbol{r}') \propto |\eta_{\rm B}(\boldsymbol{r}')|^2$ in the paraxial case (see the Supplementary Material).

In our experiment shown in Fig. 2, a femtosecond (fs) laser with a pulse duration of $\sim$140 fs, a repetition rate of 80 MHz and a wavelength of 390 nm pumps a sandwich-like type-Ⅱ crystal composed of BBO+HWP+BBO,[67] where BBO is β-BaB_2O_4 crystal and HWP is half-wave plate, respectively. The polarization-entangled photon pairs are generated by the degenerate non-collinear spontaneous parametric down-conversion (SPDC) process. We eliminate the momentum and frequency correlations of two photons using single-mode fibers (SMFs) and 3-nm narrowband filters. The obtained joint momentum spectrum exhibits a Gaussian distribution[68] as shown in the upper-right inset. After passing through the SMFs, the detected two-photon coincidence counts for the polarization entangled photon pairs is about 2.1×10^5 Hz by using two single-photon avalanche diode (SPAD) detectors (Excelitas Technologies, SPCM-780-11-FC) with a detection efficiency of $\sim$60%. The polarization entanglement fidelity of $\sim$0.982 has been achieved.

We utilize the entanglement transfer units (ETUs) composed of polarization-dependent mode-switching devices to generate the structured-phase entangled state in Eq. (1). The phases of $\Phi_{\rm A}(\boldsymbol{r})$ [its conjugate phase $-\Phi_{\rm A}(\boldsymbol{r})$] and $\Phi_{\rm B}(\boldsymbol{r}')$ [its conjugate phase $-\Phi_{\rm B}(\boldsymbol{r}')$] are applied on the photons in paths A and B, respectively, using ETU1 or ETU2 shown in the lower insets of Fig. 2. In the coincidence measurement, the idler photons in path B are filtered by a sector mask and collected by a multimode fiber (MMF), which is connected to an SPAD. The SPAD detector serves as a trigger for a pixel-intensified charge-coupled device (ICCD) camera (2DSPC-GS-F) and enables to capture the image of the spatial coincidence distribution of the signal photons in path A, i.e., $G^{(2)}(\boldsymbol{r}, \boldsymbol{r}')$ with the fixed $\boldsymbol{r}'$. The exposure time of the ICCD camera in path A keeps at $\sim$16.7 s to get a two-photon coincidence image. Considering the overall detection efficiency of $\sim$1% for the ICCD, the brightness of the photon pair detected by the ICCD and an SPAD would be 3500 Hz without inserting the fan-sector mask. The fan-sector mask in path B is scanned in the range of 2π with steps of $\pi/12$. Therefore, we need totally 24 two-photon coincidence images to reconstruct a figure of two-dimensional distribution of $g^{(2)}$, and the total measurement time is $\sim$6.7 min. The coincidence signal is influenced by the azimuthal open angle of the sector mask in path B. A larger sector will increase brightness, but it will also decrease contrast. To address the trade-off, our experiment uses a $\pi/4$-sector mask in path B instead of a very narrow one. The orientation angle of the angular bisector of the sector mask in path B is denoted by $\varphi'_{\rm M}$.

Essential Role of Quantum Entanglement. We first start with the OAM entangled state of $\frac{1}{\sqrt{2}}(|m_{\rm A}\rangle\,|{-}m_{\rm B}\rangle \pm |{-}m_{\rm A}\rangle\,|m_{\rm B}\rangle)$ to demonstrate our idea for manipulating the second-order spatial quantum coherence. It is required that the helical phases of $\Phi_{\rm A}(\boldsymbol{r}) = m_{\rm A}\varphi$ and $\Phi_{\rm B}(\boldsymbol{r}') = m_{\rm B}\varphi'$ are applied on the two photons in two paths via ETU1, where φ and φ' are the azimuthal angles in their respective polar coordinates. Based on Eq. (2), the degree of second-order spatial quantum coherence exhibits the azimuthally varying spatial structure, i.e., $g^{(2)}(\boldsymbol{r}, \boldsymbol{r}') = g^{(2)}(\varphi, \varphi') = 1 \pm \cos[2(m_{\rm A}\varphi - m_{\rm B}\varphi')]$.

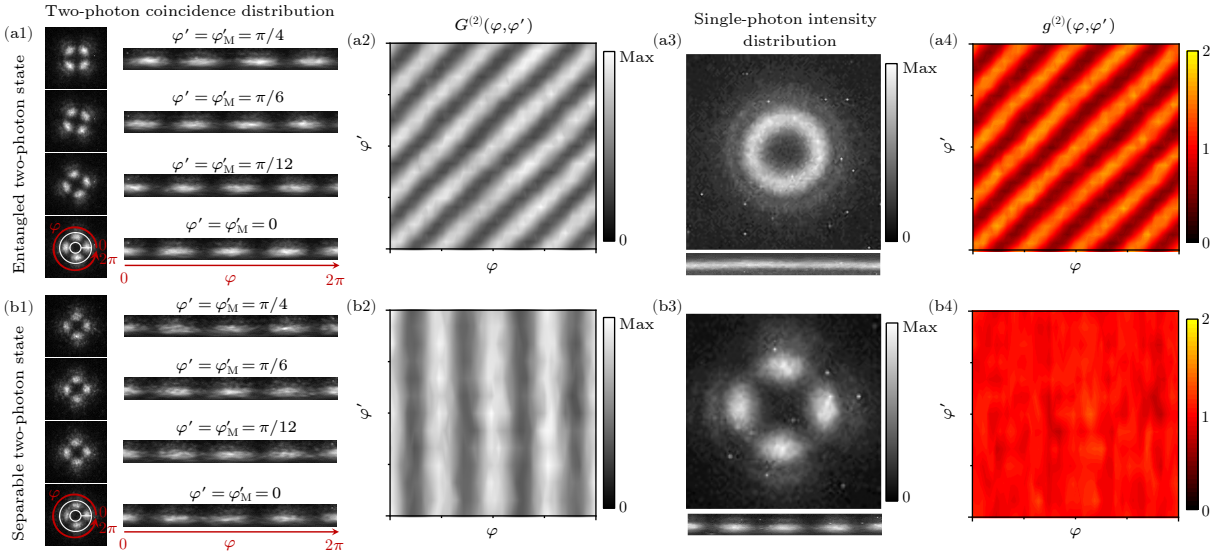

Fig. 3. Comparison of results between OAM-entangled two-photon state [(a1)–(a4)] and separable two-photon state [(b1)–(b4)]. (a1) The two-photon coincidence distributions captured by the ICCD camera in path A, triggered by the photons in path B with the sector mask at four different orientation angles ($\varphi' = \varphi'_{\rm M} = \pi/4$, $\pi/6$, $\pi/12$, 0). The right column displays the corresponding unfolded patterns of the left column. (a2) $G^{(2)}(\varphi, \varphi')$. (a3) The single-photon intensity distributions (i.e., photon numbers) in path A and its corresponding unfolded pattern displayed below. (a4) Characteristics of $g^{(2)}(\varphi, \varphi')$ with the visibility of 0.6. Since all the captions of (b1)–(b4) are completely similar to those of (a1)–(a4), they will be omitted here. Here φ and φ' take the same range of φ, $\varphi' \in [0, 2\pi]$.

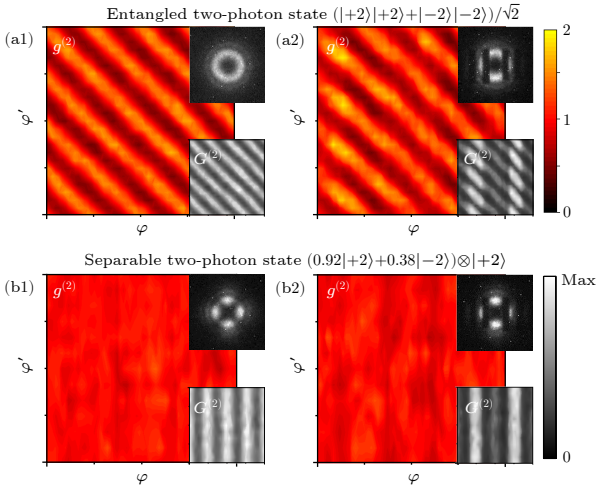

Fig. 4. Anti-intensity-disturbance of $g^{(2)}(\varphi, \varphi')$ for entangled two-photon state of $\frac{1}{\sqrt{2}}(|+2\rangle|+2\rangle + |-2\rangle|-2\rangle)$ in (a1)–(a2) and separable two-photon state of $(0.92|+2\rangle + 0.38|-2\rangle) \otimes |+2\rangle$ in (b1)–(b2). (a1) and (a2) The measured $g^{(2)}(\varphi, \varphi')$ for the entangled two-photon state when its intensity pattern is non-disturbed and disturbed by a two-stripe mask, as shown in the upper-right insets, respectively. The lower-right insets depict the corresponding $G^{(2)}(\varphi, \varphi')$ functions. We omit all the captions of (b1) and (b2) because they are similar to those of (a1) and (a2). Here φ and φ' take the same range of $\varphi, \varphi' \in [0, 2\pi]$.

To elucidate the essential role of quantum entanglement in higher-order coherence manipulation, we give a comparison with the result of the separable product state. As examples, Figs. 3(a1)–3(a4) and 3(b1)–3(b4) show the experimental results for the entangled two-photon state of $\frac{1}{\sqrt{2}}(|+2\rangle|-2\rangle + |-2\rangle|+2\rangle)$ (i.e., $m_A = m_B = 2$) and the separable two-photon state of $(0.92|+2\rangle + 0.38|-2\rangle) \otimes |+2\rangle$, respectively (see the Supplementary Material for more results). The two-photon coincidence distributions shown in Fig. 3(a1) exhibit a C_4 symmetry pattern with four petals for any fixed φ'_M, and the pattern rotates when changing φ'_M, as also shown by the unfolded patterns [69] in the right column. Based on a large number of experimental results similar to the intensity pattern shown in Fig. 3(a1) at a series of $\varphi' = \varphi'_M$, we obtain $G^{(2)}(\varphi, \varphi')$ shown in Fig. 3(a2), which exhibits a diagonal interference fringes. In Fig. 3(a3), the single-photon intensity distribution in path A has an azimuthal uniform doughnut pattern, which is different from Fig. 3(a1). In particular, $g^{(2)}(\varphi, \varphi')$ shown in Fig. 3(a4) exhibits the diagonal interference fringes with the experimental visibility of 0.6 within the range $g^{(2)} \in [0, 2]$.

For the separable product state shown in Figs. 3(b1)–3(b4), however, there are some differences from the entangled state. In Fig. 3(b1), although the two-photon coincidence distribution exhibits also a C_4 symmetry pattern but the pattern does not rotate when changing φ'_M. As shown in Fig. 3(b2), $G^{(2)}(\varphi, \varphi')$ shows vertical interference fringes. In Fig. 3(b3), the single-photon intensity in path A exhibits an azimuthal varying pattern with four petals. In contrast, in Fig. 3(b4), $g^{(2)}(\varphi, \varphi')$ is almost spatially uniform (no spatial structure) with $g^{(2)} \approx 1$. One should note that, the two-photon product state selected in experiment is $(0.92|+2\rangle + 0.38|-2\rangle) \otimes |+2\rangle$, instead of equally-weighted state (see the Supplementary Material for details). Essentially, only the first-order coherence of the product two-photon state has been modified by the helical phases.

Anti-intensity Disturbance. The $G^{(2)}$ function is susceptible to the spatial structure of first-order coherence, making it hard to precisely characterize the second-order coherence feature. In particular, we demonstrate that the $g^{(2)}$-based signal has the unique feature being the resistance to intensity disturbance as shown in Fig. 4 (see the Supplementary Material for more results). To imitate the intensity disturbance in experiment, we introduce a two-stripe translucence mask in path A. For the two-photon entangled state of $\frac{1}{\sqrt{2}}(|+2\rangle|+2\rangle + |-2\rangle|-2\rangle)$, comparing Fig. 4(a1) with Fig. 4(a2), the measured results demonstrated that $g^{(2)}$ is immune to the intensity disturbance, while $G^{(2)}$ is not. Here $g^{(2)}$ shows a diagonal fringes within a range of $g^{(2)} \in [0, 2]$. Similarly, as shown in Figs. 4(b1) and 4(b2), for the separable two-photon state of $(0.92|+2\rangle + 0.38|-2\rangle) \otimes |+2\rangle$, $g^{(2)}$ is also insensitive to the intensity disturbance, but $G^{(2)}$ is not; the measured $g^{(2)}$ has almost no spatial structure with $g^{(2)} \approx 1$.

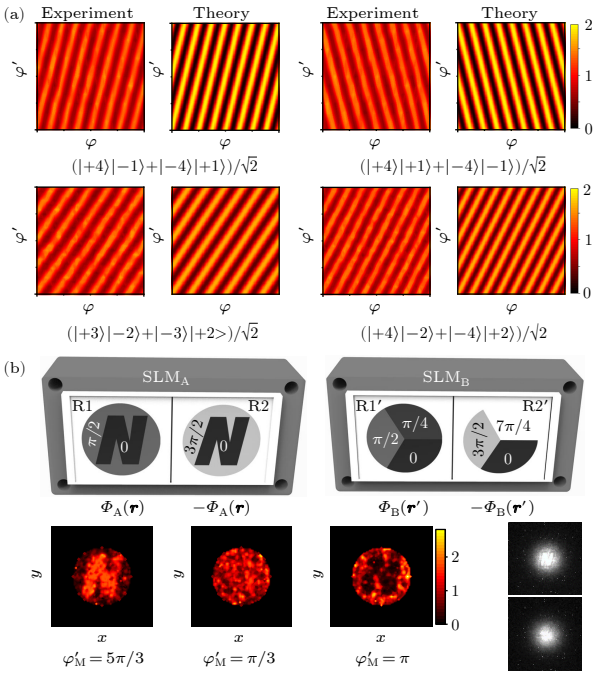

Fig. 5. Tailoring spatial quantum coherence by imposing arbitrary spatial phase structures on photons: (a) $g^{(2)}(\varphi, \varphi')$ for various OAM entangled states $\frac{1}{\sqrt{2}}(|m_A\rangle|-m_B\rangle + |-m_A\rangle|m_B\rangle)$, with $\varphi, \varphi' \in [0, 2\pi]$ with the experimental visibility of 0.5, (b) the structure-patterned $g^{(2)}$ with the letter N composed of binary-phase pattern. The first row shows the patterned phases imposed on the photons in paths A and B, by SLM_A and SLM_B. The second row gives the measured spatial patterns of $g^{(2)}$ for three different phases $\Phi_B|_{\varphi'_M=(5\pi/3,\,\pi/3,\,\pi)} = (0, \pi/4, \pi/2)$ in R1′ and $(0, 7\pi/4, 3\pi/2)$ in R2′. The photon-number densities for the photons in paths A and B are displayed in the lower-right inset.

Tailoring Spatial Quantum Coherence. Our approach for manipulating the spatial quantum coherence can be

applied to various two-photon entangled states. To confirm this, as examples of the first type, Fig. 5(a) shows the comparison between the experimental results and theoretical simulations for four different OAM-entangled states, which correspond to the entanglement situation with continuously changing phase. With the aid of ETU1 shown in Fig. 2, we carry out the experiment for obtaining the results shown in Fig. 5(a). We find that the fringe of the $g^{(2)}(\varphi, \varphi')$ pattern (with the experimental visibility of 0.5) has a period of $\pi(m_{\rm A}^2+m_{\rm B}^2)^{-1/2}$ determined by the OAM quantum numbers ($m_{\rm A}$ and $m_{\rm B}$) of the signal and idler photons. The orientation of fringes (here is defined by the fringe slope) is given by $m_{\rm A}/m_{\rm B}$ for the state of $\frac{1}{\sqrt{2}}(|m_{\rm A}\rangle|-m_{\rm B}\rangle \pm |-m_{\rm A}\rangle|m_{\rm B}\rangle)$. The visibility of the experimental obtained $g^{(2)}$ for various spatial entanglements as shown in Figs. 3 and 5 has a range from 0.5 to 0.6. The limited visibility in experiment is caused by two factors. The first factor is that the fan-sector mask utilized in path B would decrease the visibility. To obtain a bright two-photon coincidence images, we need a fan-sector mask with a larger opening angle, however, the larger opening angle will decrease the visibility. In experiment, we chose a $\pi/4$-sector mask to make a balance between brightness and visibility, which results in a theoretical visibility of 0.9 for topological charge of 1 in path B. The second factor is the shot noise on ICCD caused by the low detection efficiency when detecting a photon pair with limited brightness. In future, using a photon pair with higher brightness, which could support the utilization of a narrow fan-sector mask and suppression the shot noise, will increase the visibility of obtained $g^{(2)}$.

As examples of the second type, Fig. 5(b) shows the experimental results of the patterned-phase entangled state, corresponding to the situation with discrete changing phase. With the aid of ETU2 shown in Fig. 2, we implement the experiment for obtaining the results shown in Fig. 5(b). $\rm SLM_A$ contained in ETU2 in path A is multiplexed into two regions (R1 and R2). A binary phase distribution (0 and $\pi/2$) forms a phase-patterned letter N in R1, while the phase-patterned letter N in R2 is the conjugate of that in R1 ($3\pi/2$ is equivalent to $-\pi/2$). $\rm SLM_B$ contained in ETU2 in path B is also multiplexed into two regions (R1′ and R2′). A ternary phase distribution (0, $\pi/4$, $\pi/2$) forms a three-sector phase pattern in R1′, while the three-sector phase pattern in R2′ is the conjugate of that in R1′ ($7\pi/4$ and $3\pi/2$ are equivalent to $-\pi/4$ and $-\pi/2$, respectively). It should be noted that in ETU2, the patterned phase on the two regions R1 and R2 (R1′ and R2′) of $\rm SLM_A$ ($\rm SLM_B$) are successively mapped on the original polarization entangled photons in path A (path B), therefore, the two regions R1 and R2 (R1′ and R2′) are overlapped in path A (path B) after ETU2. By rotating the sector mask in path B, we can change the phases in R1′ and R2′ synchronously, as $\Phi_{\rm B}|_{\varphi'_{\rm M}=(5\pi/3,\,\pi/3,\,\pi)} = (0,\,\pi/4,\,\pi/2)$ in R1′ and $(0,\,7\pi/4,\,3\pi/2)$ in R2′, resulting in three distinct spatial structures of $g^{(2)}$, as shown in the second row. The observed three different $g^{(2)}(\varphi, \varphi') = 0,\,1,\,2$ for letter N represent anti-bunching, non-correlation, and bunching of two photons, respectively. Clearly, our approach enables the on-demand manipulation of second-order spatial quantum coherence of photon pairs. Single photons in paths A and B do not exhibit any spatial structure in their photon-number density distributions, as shown in the lower-right inset of Fig. 5(b). The spatial resolution of our system is fundamentally limited by the pixel sizes of SLM and ICCD, whereas the signal-to-noise ratio emerges as a more crucial limiting factor for imaging at single-photon level.[70] To improve the spatial resolution, the feasible solution is to increase the brightness of entangled photons currently.[71]

In conclusion, we have for the first time demonstrated the active manipulation of spatial structure of second-order quantum coherence in both theory and experiment. The manipulation has been achieved by mapping the entanglement of spatially structured entangled photons to the second-order spatial quantum coherence. The on-demand spatially structured entangled photons are generated by polarization-entangled photons through the entanglement transferring from polarization to OAM (using q-plates) or patterned phase (using SLMs). The experimental results clearly verify the feasibility of our approach. High-order quantum coherence in spatial domain has shown a key role in quantum applications ranging from imaging[72–76] and holography[70,77] to microscopy.[78–81] Active control of high-order spatial quantum coherence would not only enable to tap more potential in these applications but also open new opportunities for quantum information and quantum optics based on high-order coherence. Furthermore, our approach can be expanded to higher-order quantum coherence control, such as fourth-order spatial coherence of four photons (see the Supplementary Material).

Acknowledgments. This work was supported by the National Natural Science Foundation of China (Grant Nos. 12234009, 12275048, 12304359, and 12274215), the National Key R&D Program of China (Grant No. 2020YFA0309500), the Innovation Program for Quantum Science and Technology (Grant No. 2021ZD0301400), the Program for Innovative Talents and Entrepreneurs in Jiangsu, the Natural Science Foundation of Jiangsu Province (Grant No. BK20220759), the Key R&D Program of Guangdong Province, China (Grant No. 2020B0303010001), the China Postdoctoral Science Foundation (Grant No. 2023M731611), and the Jiangsu Funding Program for Excellent Postdoctoral Talent (Grant No. 2023ZB717).

References

[1] Hanbury Brown R and Twiss R Q 1956 *Nature* **177** 27
[2] Glauber R J 1963 *Phys. Rev.* **130** 2529
[3] Hanbury Brown R and Twiss R Q 1956 *Nature* **178** 1046
[4] Bromberg Y, Lahini Y, Small E, and Silberberg Y 2010 *Nat. Photon.* **4** 721
[5] Magaña-Loaiza O S, Mirhosseini M, Cross R M, Rafsanjani S M H, and Boyd R W 2016 *Sci. Adv.* **2** e1501143
[6] Henny M, Oberholzer S, Strunk C, Heinzel T, Ensslin K, Holland M, and Schönenberger C 1999 *Science* **284** 296
[7] Oliver W D, Kim J, Liu R C, and Yamamoto Y 1999 *Science* **284** 299
[8] Schellekens M, Hoppeler R, Perrin A, Gomes J V, Boiron D, Aspect A, and Westbrook C I 2005 *Science* **310** 648

[9] Öttl A, Ritter S, Köhl M, and Esslinger T 2005 *Phys. Rev. Lett.* **95** 090404

[10] Jeltes T, McNamara J M, Hogervorst W, Vassen W, Krachmalnicoff V, Schellekens M, Perrin A, Chang H, Boiron D, Aspect A, and Westbrook C I 2007 *Nature* **445** 402

[11] Rosenberg J S, Christakis L, Guardado-Sanchez E, Yan Z Z, and Bakr W S 2022 *Nat. Phys.* **18** 1062

[12] Perrin A, Bücker R, Manz S, Betz T, Koller C, Plisson T, Schumm T, and Schmiedmayer J 2012 *Nat. Phys.* **8** 195

[13] Cayla H, Butera S, Carcy C, Tenart A, Hercé G, Mancini M, Aspect A, Carusotto I, and Clément D 2020 *Phys. Rev. Lett.* **125** 165301

[14] He Y M, He Y, Wei Y J, Wu D, Atatüre M, Schneider C, Höfling S, Kamp M, Lu C Y, and Pan J W 2013 *Nat. Nanotechnol.* **8** 213

[15] Ding X, He Y, Duan Z C, Gregersen N, Chen M C, Unsleber S, Maier S, Schneider C, Kamp M, Höfling S, Lu C Y, and Pan J W 2016 *Phys. Rev. Lett.* **116** 020401

[16] Somaschi N, Giesz V, De Santis L, Loredo J C, Almeida M P, Hornecker G, Portalupi S L, Grange T, Antón C, Demory J, Gómez C, Sagnes I, Lanzillotti-Kimura N D, Lemaítre A, Auffeves A, White A G, Lanco L, and Senellart P 2016 *Nat. Photon.* **10** 340

[17] Tomm N, Javadi A, Antoniadis N O, Najer D, Löbl M C, Korsch A R, Schott R, Valentin S R, Wieck A D, Ludwig A, and Warburton R J 2021 *Nat. Nanotechnol.* **16** 399

[18] Tang J S, Li Y L, Xu X Y, Xiang G Y, Li C F, and Guo G C 2012 *Nat. Photon.* **6** 600

[19] Wen Y L, Wang Y F, Tian L M, Zhang S C, Li J F, Du J S, Yan H, and Zhu S L 2023 *Nat. Photon.* **17** 717

[20] Lu C Y and Pan J W 2021 *Nat. Nanotechnol.* **16** 1294

[21] Chu X L, Götzinger S, and Sandoghdar V 2017 *Nat. Photon.* **11** 58

[22] Wang H, Qin J, Chen S, Chen M C, You X, Ding X, Huo Y H, Yu Y, Schneider C, Höfling S, Scully M, Lu C Y, and Pan J W 2020 *Phys. Rev. Lett.* **125** 153601

[23] Wang H, Qin J, Ding X, Chen M C, Chen S, You X, He Y M, Jiang X, You L, Wang Z, Schneider C, Renema J J, Höfling S, Lu C Y, and Pan J W 2019 *Phys. Rev. Lett.* **123** 250503

[24] Cogan D, Su Z E, Kenneth O, and Gershoni D 2023 *Nat. Photon.* **17** 324

[25] Short R and Mandel L 1983 *Phys. Rev. Lett.* **51** 384

[26] Nogueira W A T, Walborn S P, Pádua S, and Monken C H 2001 *Phys. Rev. Lett.* **86** 4009

[27] Liu R, Kong L J, Si Y, Wang Z X, Qi W R, Tu C H, Li Y N, and Wang H T 2019 *Chin. Phys. Lett.* **36** 044205

[28] Nogueira W A T, Walborn S P, Pádua S, and Monken C H 2004 *Phys. Rev. Lett.* **92** 043602

[29] Wolf S, Richter S, von Zanthier J, and Schmidt-Kaler F 2020 *Phys. Rev. Lett.* **124** 063603

[30] Valencia A, Scarcelli G, D'Angelo M, and Shih Y 2005 *Phys. Rev. Lett.* **94** 063601

[31] Si Y, Kong L J, Li Y N, Tu C H, and Wang H T 2016 *Chin. Phys. Lett.* **33** 034203

[32] Oppel S, Büttner T, Kok P, and von Zanthier J 2012 *Phys. Rev. Lett.* **109** 233603

[33] Strekalov D V, Sergienko A V, Klyshko D N, and Shih Y H 1995 *Phys. Rev. Lett.* **74** 3600

[34] Bennink R S, Bentley S J, and Boyd R W 2002 *Phys. Rev. Lett.* **89** 113601

[35] Zhao S M, Ding J, Dong X L, and Zheng B Y 2011 *Chin. Phys. Lett.* **28** 124207

[36] Gatti A, Brambilla E, Bache M, and Lugiato L A 2004 *Phys. Rev. Lett.* **93** 093602

[37] Malik M, Shin H, O'Sullivan M, Zerom P, and Boyd R W 2010 *Phys. Rev. Lett.* **104** 163602

[38] Zia D, Dehghan N, D'Errico A, Sciarrino F, and Karimi E 2023 *Nat. Photon.* **17** 1009

[39] Cameron P, Courme B, Vernière C, Pandya R, Faccio D, and Defienne H 2024 *Science* **383** 1142

[40] Mair A, Vaziri A, Weihs G, and Zeilinger A 2001 *Nature* **412** 313

[41] Kovlakov E V, Bobrov I B, Straupe S S, and Kulik S P 2017 *Phys. Rev. Lett.* **118** 030503

[42] Defienne H, Reichert M, and Fleischer J W 2018 *Phys. Rev. Lett.* **121** 233601

[43] Erhard M, Krenn M, and Zeilinger A 2020 *Nat. Rev. Phys.* **2** 365

[44] Forbes A, de Oliveira M, and Dennis M R 2021 *Nat. Photon.* **15** 253

[45] Gao X, Zhang Y, D'Errico A, Sit A, Heshami K, and Karimi E 2024 *Phys. Rev. Lett.* **132** 063802

[46] Dada A C, Leach J, Buller G S, Padgett M J, and Andersson E 2011 *Nat. Phys.* **7** 677

[47] Zhang Y, Roux F S, Konrad T, Agnew M, Leach J, and Forbes A 2016 *Sci. Adv.* **2** e1501165

[48] Hiesmayr B C, de Dood M J A, and Löffler W 2016 *Phys. Rev. Lett.* **116** 073601

[49] Malik M, Erhard M, Huber M, Krenn M, Fickler R, and Zeilinger A 2016 *Nat. Photon.* **10** 248

[50] Zhang Y, Agnew M, Roger T, Roux F S, Konrad T, Faccio D, Leach J, and Forbes A 2017 *Nat. Commun.* **8** 632

[51] Erhard M, Malik M, Krenn M, and Zeilinger A 2018 *Nat. Photon.* **12** 759

[52] Fickler R, Lapkiewicz R, Plick W N, Krenn M, Schaeff C, Ramelow S, and Zeilinger A 2012 *Science* **338** 640

[53] Hiekkamäki M, Bouchard F, and Fickler R 2021 *Phys. Rev. Lett.* **127** 263601

[54] Barreiro J T, Langford N K, Peters N A, and Kwiat P G 2005 *Phys. Rev. Lett.* **95** 260501

[55] Kong L J, Liu R, Qi W R, Wang Z X, Huang S Y, Tu C H, Li Y N, and Wang H T 2020 *Chin. Phys. Lett.* **37** 034204

[56] Zhao T M, Ihn Y S, and Kim Y H 2019 *Phys. Rev. Lett.* **122** 123607

[57] Barreiro J T, Wei T C, and Kwiat P G 2008 *Nat. Phys.* **4** 282

[58] Li Y, Huang S Y, Wang M, Tu C H, Wang X L, Li Y N, and Wang H T 2023 *Phys. Rev. Lett.* **130** 050805

[59] D'Ambrosio V, Nagali E, Walborn S P, Aolita L, Slussarenko S, Marrucci L, and Sciarrino F 2012 *Nat. Commun.* **3** 961

[60] Zhao S M, Gong L Y, Li Y Q, Yang H, Sheng Y B, and Cheng W W 2013 *Chin. Phys. Lett.* **30** 060305

[61] Graham T M, Barreiro J T, Mohseni M, and Kwiat P G 2013 *Phys. Rev. Lett.* **110** 060404

[62] Wang X L, Cai X D, Su Z E, Chen M C, Wu D, Li L, Liu N L, Lu C Y, and Pan J W 2015 *Nature* **518** 516

[63] Liu Z F, Chen C, Xu J M, Cheng Z M, Ren Z C, Dong B W, Lou Y C, Yang Y X, Xue S T, Liu Z H, Zhu W Z, Wang X L, and Wang H T 2022 *Phys. Rev. Lett.* **129** 263602

[64] Mirhosseini M, Magaña-Loaiza O S, Chen C C, Hashemi Rafsanjani S M, and Boyd R W 2016 *Phys. Rev. Lett.* **116** 130402

[65] Yang L P and Xu D 2022 *Phys. Rev. A* **105** 023723

[66] Cui D Z, Wang X L, Yi X X, and Yang L P 2024 *Phys. Rev. Appl.* **21** 024019

[67] Wang X L, Chen L K, Li W, Huang H L, Liu C, Chen C, Luo Y H, Su Z E, Wu D, Li Z D, Lu H, Hu Y, Jiang X, Peng C Z, Li L, Liu N L, Chen Y A, Lu C Y, and Pan J W 2016 *Phys. Rev. Lett.* **117** 210502

[68] Walborn S P, Monken C H, Pádua S, and Souto Ribeiro P H 2010 *Phys. Rep.* **495** 87

[69] Moreau P A, Toninelli E, Gregory T, Aspden R S, Morris P A, and Padgett M J 2019 *Sci. Adv.* **5** eaaw2563

[70] Defienne H, Ndagano B, Lyons A, and Faccio D 2021 *Nat. Phys.* **17** 591
[71] Zhong H S, Wang H, Deng Y H, Chen M C, Peng L C, Luo Y H, Qin J, Wu D, Ding X, Hu Y, Hu P, Yang X Y, Zhang W J, Li H, Li Y X, Jiang X, Gan L, Yang G W, You L X, Wang Z, Li L, Liu N L, Lu C Y, and Pan J W 2020 *Science* **370** 1460
[72] Cui D, Yi X, and Yang L P 2023 *Adv. Quantum Technol.* **6** 2370053
[73] Edgar M P, Tasca D S, Izdebski F, Warburton R E, Leach J, Agnew M, Buller G S, Boyd R W, and Padgett M J 2012 *Nat. Commun.* **3** 984
[74] Defienne H, Reichert M, and Fleischer J W 2018 *Phys. Rev. Lett.* **120** 203604
[75] Moreau P A, Toninelli E, Gregory T, and Padgett M J 2019 *Nat. Rev. Phys.* **1** 367
[76] Defienne H, Zhao J, Charbon E, and Faccio D 2021 *Phys. Rev. A* **103** 042608
[77] Chrapkiewicz R, Jachura M, Banaszek K, and Wasilewski W 2016 *Nat. Photon.* **10** 576
[78] Tenne R, Rossman U, Rephael B, Israel Y, Krupinski-Ptaszek A, Lapkiewicz R, Silberberg Y, and Oron D 2019 *Nat. Photon.* **13** 116
[79] Varnavski O and Goodson T 2020 *J. Am. Chem. Soc.* **142** 12966
[80] Lubin G, Oron D, Rossman U, Tenne R, and Yallapragada V J 2022 *ACS Photon.* **9** 2891
[81] Ndagano B, Defienne H, Branford D, Shah Y D, Lyons A, Westerberg N, Gauger E M, and Faccio D 2022 *Nat. Photon.* **16** 384